RSC Advances

RSC Publishing

PAPER

View Article Online
View Journal | View Issue

Cite this: *RSC Advances*, 2013, **3**, 16542

Synthesis and improved electrochemical performances of nano β-$NiMoO_4$–$CoMoO_4 \cdot xH_2O$ composites for asymmetric supercapacitors†

Baskar Senthilkumar,[ab] Danielle Meyrick,*[b] Yun-Sung Lee[c] and Ramakrishnan Kalai Selvan*[a]

Received 17th June 2013,
Accepted 4th July 2013

DOI: 10.1039/c3ra43021a

www.rsc.org/advances

Nano-sized β-$NiMoO_4$–$CoMoO_4 \cdot xH_2O$ composites were synthesized by a solution combustion synthesis (SCS) technique. The effect of weight ratio of transition metal on the electrochemical capacitive performance of the nanocomposites was investigated by cyclic voltammetry and galvanostatic charge–discharge methods. The $NiMoO_4$–$CoMoO_4 \cdot xH_2O$ nanocomposite with weight ratio of 3 : 1 (Ni : Co) exhibits enhanced capacitive behaviour relative to other composites and delivered a maximum specific capacitance of 1472 Fg^{-1} at a current density of 5 $mAcm^{-2}$. The enhancement in specific capacitance is due to the small particle size, uniform size distribution, high surface area and high weight fraction of Ni. The synergistic effect of nickel and cobalt improves the electrochemical behaviour relative to pure nickel and cobalt molybdates. A full cell was fabricated using the β-$NiMoO_4$–$CoMoO_4 \cdot xH_2O$ nanocomposite (3 : 1) and activated carbon (AC) as a positive and negative electrode, respectively. The cell delivered high capacitance (80 Fg^{-1}) and energy density (28 Wh kg^{-1}) and good cycling stability up to 1000 cycles.

1. Introduction

Metal molybdates are an important class of semiconducting materials widely used in catalysis,[1] photoluminescence,[2] sensors,[3] magnetic[4] and energy storage applications.[5–14] In recent years these materials have received significant interest for their use as electrode materials for Li-ion batteries[5–7] and supercapacitors.[8–14] Very recently, Haetge *et al.* has prepared nanocrystalline $NiMoO_4$ with an ordered mesoporous structure.[5] The material exhibits an initial discharge capacity of 270 mA h g^{-1}.[5] Purushothaman *et al.* have synthesized α-$MnMoO_4$ by using the sol–gel spin coating method and obtained a specific capacitance of 998, 784 and 530 F g^{-1} in H_2SO_4, *para*-toluene sulfonic acid (*P*-TSA) and HCl electrolytes respectively.[8] Xu *et al.* demonstrated a specific capacitance of 170 F g^{-1} for microwave synthesized $CoMoO_4$/MWCNTs at 1 A g^{-1},[9] while Liu *et al.* reported a high capacitance of 326 F g^{-1} at 5 mA cm^{-2} for $CoMoO_4 \cdot 0.9H_2O$ synthesized by a hydrothermal process.[10] In our recent work on combustion synthesized metal molybdates, $MnMoO_4$, $CoMoO_4 \cdot xH_2O$ and $NiMoO_4$ provided a high specific capacitance at 5 mA cm^{-2} of 126, 401 and 1116 Fg^{-1} respectively.[11] Hierarchical bismuth molybdate nanowires prepared by a facile electrodeposition-heat method demonstrated its suitability as a negative electrode material for supercapacitors, exhibiting a capacitance of 1075 Fg^{-1} at 1 Ag^{-1} and excellent cycle life up to 1000 cycles.[12]

Mixed metal molybdates have also been studied as electrode materials for Li-ion batteries and supercapacitors.[13–15] Mixed metal molybdates provide an improvement in electrochemical performance due to the synergistic effect of individual metal molybdates.[13–15] For example, compared to $CoMoO_4$ (290 mA h g^{-1}) nanowires synthesised by a hydrothermal method, $Ni_{0.75}Co_{0.25}MoO_4$ nanowires exhibited reversible capacity of 520 $mAhg^{-1}$ after 20 cycles.[13] Mai *et al.* synthesized heterostructured $MnMoO_4$–$CoMoO_4$ nanowires by a micro-emulsion method and studied their capacitance behavior.[14] Heterostructured $MnMoO_4$–$CoMoO_4$ nanowires show a capacitance of 187.1 Fg^{-1} and excellent cycling stability. This capacitance value is higher than $MnMoO_4$ (9.7 Fg^{-1}) and $CoMoO_4$ (62.8 Fg^{-1}).[14] More recently, Liu *et al.* demonstrated an improvement in electrochemical performance for $CoMoO_4$–$NiMoO_4 \cdot xH_2O$ bundles compared to the corresponding individual metal molybdates.[15] The composite synthesized with Ni–Co mass ratio of 1.4 : 0.6 showed the advantage of both $NiMoO_4 \cdot xH_2O$ (high specific capacitance, 1039 Fg^{-1}) and $CoMoO_4$ (rate capability).[15]

[a]*Solid State Ionics & Energy Devices Laboratory, Department of Physics, Bharathiar University, Coimbatore 641 046, India. E-mail: selvankram@buc.edu.in; Tel: +91-422-2428446*

[b]*School of Chemical and Mathematical Sciences, Murdoch University, Murdoch, WA 6150, Australia. E-mail: d.meyrick@murdoch.edu.au*

[c]*Faculty of Applied Chemical Engneering, Chonnam National University, Gwangju 500-757, Korea*

† Electronic supplementary information (ESI) available. See DOI: 10.1039/c3ra43021a

For improved electrochemical performance, preparation of material within the nanometre size range is required.[16–18] It is believed that nanostructures improve the electrochemical performance due to the increase in surface area and active sites of the electrode material and a decrease in diffusion distance of the electrolyte.[16–18] The interesting results on mixed metal molybdates, particularly high specific capacitance of $NiMoO_4$ (1517 Fg^{-1})[11] and high rate capability and cycling stability of $CoMoO_4$ motivated us to work on $NiMoO_4$–$CoMoO_4$ nanocomposites.[9–11,14,15] In this present work, we have prepared nano-sized β-$NiMoO_4$–$CoMoO_4{\cdot}xH_2O$ composites with three different Ni : Co weight ratios (3 : 1, 1 : 1 and 1 : 3) by a solution combustion synthesis (SCS) technique. We have studied the structural, morphological and electrochemical properties of the nanocomposites. The effect of weight ratio on the electrochemical capacitive performances was also investigated. The $NiMoO_4$–$CoMoO_4{\cdot}xH_2O$ nanocomposite with Ni : Co ratio 3 : 1 exhibits enhanced capacitance of 1472 Fg^{-1}, compared to other samples (1 : 1 and 1 : 3). The enhancement in electrochemical capacitance behaviour of the material is due to the small particle size, uniform size distribution, high surface area and high weight fraction of Ni. A full cell (AC||$NiMoO_4$–$CoMoO_4{\cdot}xH_2O$) was fabricated, and delivered good electrochemical performance relative to the reported work based on molybdate.[15]

2. Experimental

Material synthesis

All chemicals were purchased from Aldrich and used as received without further purification. For a typical synthesis of $NiMoO_4$–$CoMoO_4{\cdot}xH_2O$ with Ni : Co weight ratio of 3 : 1, $Ni(NO_3)_2{\cdot}6H_2O$ (1.995 g), $Co(NO_3)_2{\cdot}6H_2O$ (0.665 g), $(NH_4)_6Mo_7O_{24}{\cdot}4H_2O$ (1.615 g) and Urea–$CO(NH_2)_2$ (0.68 g) were used. Urea was used as fuel and the oxidant-to-fuel ratio was maintained at one. Precursors were dissolved in 5 mL of distilled water separately. The solutions were mixed, and the pH adjusted to ~8 by drop-wise addition of ammonia. The resulting solution was placed on a hot plate and maintained at a temperature around 200 °C. After complete dehydration, the remaining solid mass was transferred to a muffle furnace and the temperature was raised to 300 °C. After a few minutes, decomposition with gradual release of gases was observed. Finally, a foamy powder of β-$NiMoO_4$–$CoMoO_4{\cdot}xH_2O$ was collected and ground in an agate mortar. A similar procedure was repeated for the preparation of $NiMoO_4$–$CoMoO_4{\cdot}xH_2O$ with Ni : Co weight ratios of 1 : 1 and 1 : 3. The samples were calcined at 300 °C for 3 h.

Characterization

Thermogravimetric analysis (TGA) was carried out by Perkin Elmer STA 6000 thermo-balance at a heating rate of 15 °C min^{-1} in a static air atmosphere. Phase formation was identified by powder X-ray diffractometer 5635 (Siemens, D500 advance) with Cu Kα radiation. To investigate the morphology of the prepared samples, high magnification with a Zeiss Neon 40EsB focussed ion beam-scanning electron microscope (FIB-SEM) was used. The surface area and pore distribution of the composites were investigated by N_2 adsorption–desorption experiments at 77 K using a Micromeritics ASAP 2010 surface area analyser. The cyclic voltammetry and galvanostatic charge–discharge studies of the composites were carried out using SP-150, Bio-Logic Science Instruments in 2 M NaOH electrolyte at room temperature. To prepare active electrode material, $NiMoO_4$–$CoMoO_4{\cdot}xH_2O$ (85 wt%), carbon black (10 wt%) and polyvinlidene fluoride (PVDF) (5 wt%) were suspended in 0.4 mL of N-methyl-2-pyrrolidinone (NMP) to form a slurry. The slurry was coated on a small piece of graphite sheet (area of coating, 1 cm^2). The loaded active material was approximately 2 mg in each case. Activated carbon (AC) was purchased from Aldrich, and had a surface area of ~1800 m^2g^{-1}. To prepare the active negative electrode material, AC (90 wt%) and polyvinlidene fluoride (PVDF) (10 wt%) were used. A full cell (AC||$NiMoO_4$–$CoMoO_4{\cdot}xH_2O$) was fabricated employing a polypropylene separator. The active material loading was adjusted to a 3 : 1 (AC:$NiMoO_4$–$CoMoO_4{\cdot}xH_2O$) ratio.

3. Results and discussion

Combustion synthesis has advantages of short reaction time and high reaction temperature. The equipment needed is simple and cost-effective. Combustion synthesis is a possible preparation technique for nano-sized porous metal oxides[19–22] thus we have selected this method for the preparation of our $NiMoO_4$–$CoMoO_4{\cdot}xH_2O$ nanocomposites. Among three different crystalline phases of $NiMoO_4$, α and β phases are the most stable under standard pressure conditions.[23a] The β phase $NiMoO_4$ is highly active and selective in some catalysed reactions.[23b] Preparation of β-$NiMoO_4$ is mainly dependent upon the sample reaction conditions. In the present work, pure β-$NiMoO_4$ is achieved by combustion synthesis in the presence of Co^{2+} ions. In our earlier work, α-$NiMoO_4$ is formed under the same conditions in the absence of the cobalt precursors. The exothermic reaction of the nitrate precursors and urea is the reason for the formation high temperature phase of β-$NiMoO_4$.[23a] which is stabilized by the presence of cobalt precursors. To understand the synthesis stages and thermal behaviour of the product, we have carried out thermal gravimetric analysis for the mixed precursors. A typical TGA curve of mixed precursors for the preparation of $NiMoO_4$–$CoMoO_4{\cdot}xH_2O$ nanocomposite (1 : 1) is shown in Fig. 1. Three weight loss steps are observed. The initial weight loss (~6 wt%) at 100–190 °C is due to the loss of physisorbed water molecules. Further weight loss at 190–260 °C accompanies the decomposition of the reactants. Substantial weight loss (~33 wt%) at around 305 °C is attributed to exothermic combustion reaction.[22] There is no significant weight loss after 305 °C, suggesting the formation of stable products. The endothermic peak centered at 150 °C in the DTA curve is due to the removal of physisorbed water. An exothermic peak at 305 °C corresponds to the combustion of carbonaceous products, such as

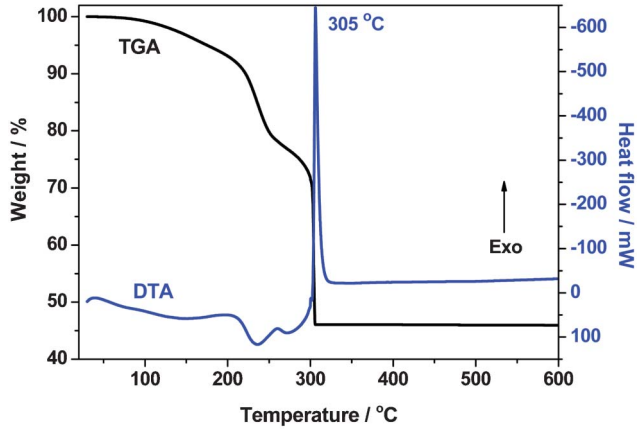

Fig. 1 TG/DTA of the mixed precursors.

residual urea. The peaks further confirm the stages of the synthesis process.

XRD patterns of combustion synthesized β-$NiMoO_4$–$CoMoO_4{\cdot}xH_2O$ nanocomposites with different Ni : Co weight ratios were recorded (Fig. 2). The diffraction peaks of the composites are well matched with the standard diffraction patterns of β-$NiMoO_4$ (JCPDS no. 45-0142) and $CoMoO_4{\cdot}xH_2O$ (JCPDS no. 26-0477). There are no impurity peaks, such as those for NiO or MoO_3, observed. Preparation of pure $NiMoO_4$ devoid of any structural hydrates is possible by combustion synthesis without any calcination.[11,23] This is not, however, possible for $CoMoO_4$, since its hydrate structure forms very easily.[9,24,25] The grain size (Table 1) was calculated by the Scherrer formula using the high intensity diffraction peak (220). The diffraction pattern of β-$NiMoO_4$–$CoMoO_4{\cdot}xH_2O$ nanocomposite with 3 : 1 (Ni : Co) ratio is indicative of a more amorphous product, and the calculated grain size is small (46 nm) relative to other composites. The poor crystallization of the composite may provide more conducting pathways compared to crystalline samples.[15,26]

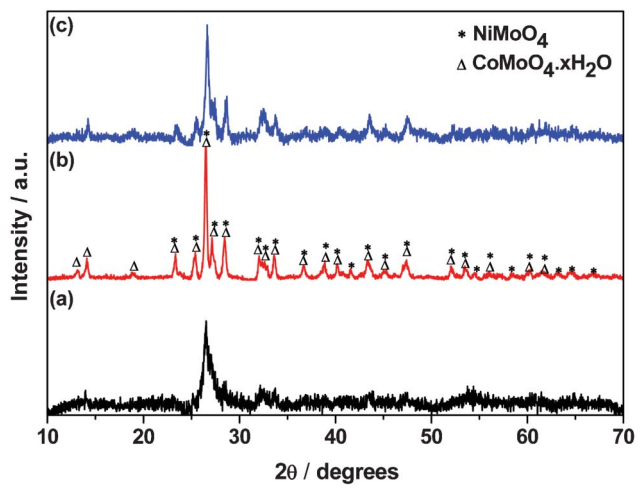

Fig. 2 XRD pattern of combustion synthesized $NiMoO_4$–$CoMoO_4{\cdot}xH_2O$ nanocomposites with Ni : Co ratio of 3 : 1 (a), 1 : 1 (b) and 1 : 3 (c).

The FTIR spectrum of $NiMoO_4$–$CoMoO_4{\cdot}xH_2O$ nanocomposites are shown in Fig. S1, ESI.† The peaks are observed at 1625, 1385, 950, 791 and 654 cm^{-1}. The peak at 1625 cm^{-1} is due to OH stretching vibrations of the physisorbed water molecules. The presence of carbon (from urea) is identified from the peak at 1385 cm^{-1}, which is due to the C–O stretching vibration.[11] The characteristic absorption peaks of β-$NiMoO_4$ are observed at 955, 800 and 690 cm^{-1}. A peak at 878 cm^{-1}, characteristic of β-$NiMoO_4$[23,27] was observed only for high Ni concentrated samples (3 : 1 and 1 : 1).

FIB-SEM images of combustion synthesized $NiMoO_4$–$CoMoO_4{\cdot}xH_2O$ nanocomposites are shown in Fig. 3. The prepared particles are in the nanometer range with grain-like morphology. The composite with Ni : Co ratio of 3 : 1 (Fig. 3(a,b)) displayed particularly small, highly agglomerated β-$NiMoO_4$–$CoMoO_4{\cdot}xH_2O$ particles. The agglomeration of these small grains creates a porous structure. The particle size distribution (Table 1) was measured using Scion image software. An increase in particle size and less agglomeration was observed as the Ni to Co mass ratio decreased, due to the increment in structural parameters (lattice constants) of $CoMoO_4{\cdot}xH_2O$.[10,15] The nanostructures may yield improved electrochemical performance due to an increase in surface area and number of active sites of the electrode material and decrease in diffusion path length.[16–18] The elemental compositions of the $NiMoO_4$–$CoMoO_4{\cdot}xH_2O$ nanocomposites were determined by energy dispersive X-ray spectroscopy (EDS) which is shown in Fig. S2, ESI.† Strong peaks of Ni, Co, Mo and O were observed. The observed atomic ratio of Ni, Co, Mo and O (~1 : 1 : 2 : 8) are matched with the stoichiometry of the compounds. Elemental mapping of the composites is presented in Fig. S3–S5, ESI,† showing a uniform distribution of elements in the composites.

The N_2 adsorption–desorption isotherms and pore size distributions (BJH-plot) of the as prepared $NiMoO_4$–$CoMoO_4{\cdot}xH_2O$ nanocomposites are shown in Fig. 4. The observed Type IV isotherm and BJH-plot for the samples with Ni : Co ratio of 3 : 1 and 1 : 1 confirms the presence of mesopores. The observed Brunauer-Emmett-Teller (BET) surface areas, total pore volumes (V_p) and average pore sizes (d_p) are given in Table 1. The calculated surface area of the samples is higher than that for reported $CoMoO_4$–$NiMoO_4{\cdot}xH_2O$ composites.[15] The increase in surface area is due to the small particle size of the composites (3 : 1). The pore size distributions of the samples are calculated using the Barrett-Joyner-Halenda (BJH) method. The obtained average pore diameter of ~ 15 nm to 24 nm of the composites (Table 1) indicates the presence of mesopores, which facilitate electrolyte ion diffusion by providing an increase in active sites.

The electrochemical capacitance performance of the materials was determined from cyclic voltammetry (CV) carried out using a platinum wire as a counter electrode and Hg/HgO as a reference electrode. An aqueous solution of 2 M NaOH was used as electrolyte. The CV curves of $NiMoO_4$–

Table 1 Physicochemical parameters

Ni : Co	Grain size (XRD) nm	Particle size (SEM) nm	z	S_{BET} m^2g^{-1}	V_p cm^3g^{-1}	d_p nm	Capacitance (2 mVs^{-1}) Fg^{-1}
3 : 1	46	10–55	2.7	18.7	0.07	15.7	1928
1 : 1	66	13–74	1.8	22.6	0.09	15.3	1259
1 : 3	78	24–120	1.0	17.7	0.11	24.7	699

$CoMoO_4{\cdot}xH_2O$ nanocomposites at a scan rate of 2 mV s^{-1} are shown in Fig. 5(a). Well-defined redox peaks were observed for the nanocomposites. The prominent redox peaks observed in the CV curves are due to the following diffusion controlled reversible redox reaction[11]

$$Ni(II) \leftrightarrow Ni(III) + e^- \quad (1)$$

For samples with higher Co mass ratio (1 : 3, Ni : Co) an additional oxidation peak due to the oxidation of Co(II) to Co(III)[11] was identified at 0.25 V *vs.* Hg/HgO. When compared to other composites, $NiMoO_4$–$CoMoO_4{\cdot}xH_2O$ with Ni : Co ratio of 3 : 1 delivered a high peak current value and a large current area under the curve, indicating the energy stored by the active material (3 : 1) is high.

The specific capacitance of the material was calculated using the relation, $C = \frac{\int Idv}{2mv\Delta V}$, where I, m, v and ΔV represent current, mass of the active material, scan rate and potential window, respectively. The calculated capacitance and active site (z) value[28] for the nanocomposites are given in Table 1. The highest capacitance (1928 Fg^{-1}) is achieved by $NiMoO_4$–$CoMoO_4{\cdot}xH_2O$ with Ni : Co ratio of 3 : 1, which is likely due to the greater surface area and more number of active sites (2.7) of the electrode material for this sample, and the high concentration of Ni.[11] The CV curves of $NiMoO_4$–$CoMoO_4{\cdot}xH_2O$ nanocomposites at various scan rates (2–20 mVs^{-1}) are given in Fig. 5(b). The well-defined redox peaks were observed even at a high scan rate of 20 mVs^{-1}, revealing the high rate capability and good reversibility of the material. The reproducibility of redox peaks further confirms that the electronic and ionic transport of the material is rapid enough at the given scan rates.[10,11,14]

Galvanostatic charge–discharge curves of the $NiMoO_4$–$CoMoO_4{\cdot}xH_2O$ nanocomposite (3 : 1) at various current densities are shown in Fig. 5(c). The pseudo-capacitive nature of the material was displayed by quasi-symmetric charge–discharge profile. The specific capacitance (C) of the electrodes is calculated using the equation,[16] $C = \frac{I}{m(dv/dt)}$ where, I is the current density, dv/dt is the average slope of the discharge curve and m is mass of the active electrode material. The specific capacitance values calculated from the discharge curves of the $NiMoO_4$–$CoMoO_4{\cdot}xH_2O$ composites at various current densities are shown in Fig. 5(d). A maximum capacitance (1472 Fg^{-1}) was observed for the 3 : 1 composite at a current density of 5 mA cm^{-2}. The capacitance value is comparatively higher than the reported values of $MnMoO_4$,[8,11,14] $NiMoO_4$,[11] $CoMoO_4$,[10,11,14]

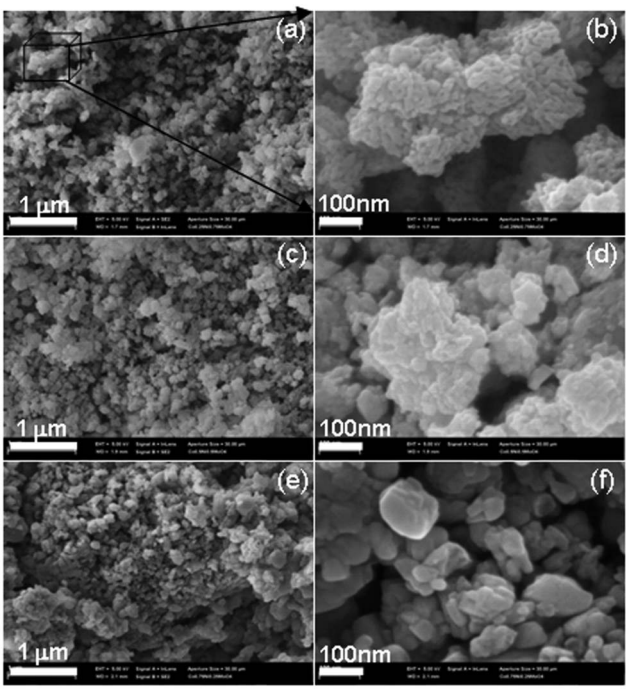

Fig. 3 FIB-SEM images of the combustion synthesized $NiMoO_4$–$CoMoO_4{\cdot}xH_2O$ nanocomposites with Ni : Co ratio of 3 : 1 (a, b), 1 : 1 (c, d) and 1 : 3 (e,f).

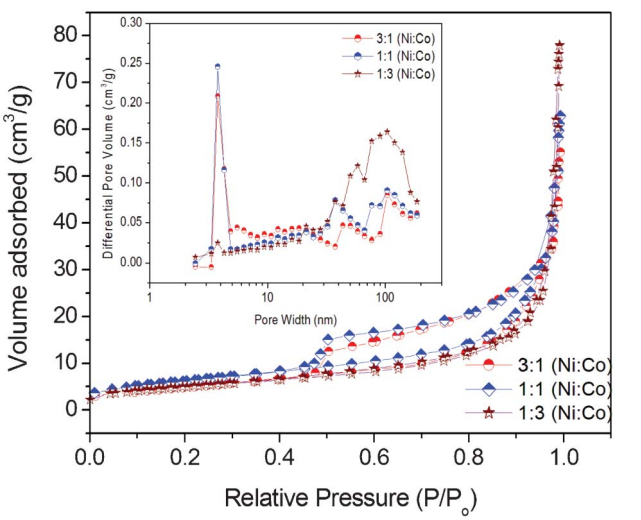

Fig. 4 N_2 adsorption–desorption isotherms and (inset) pore-size distributions of $NiMoO_4$–$CoMoO_4{\cdot}xH_2O$ nanocomposites.

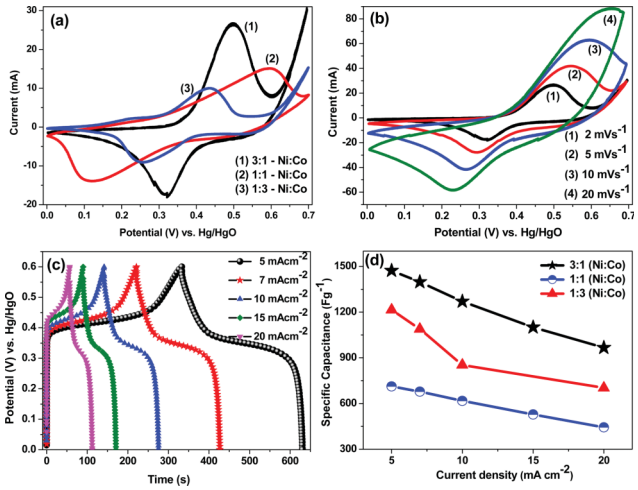

Fig. 5 CV curves at a scan rate of 2 mV s^{-1} (a). CV curves (b) and charge–discharge curves (c) of combustion synthesized $NiMoO_4$–$CoMoO_4{\cdot}xH_2O$ nanocomposites with Ni : Co ratio of 3 : 1 and specific capacitance *vs.* current densities of the nanocomposites.

$MnMoO_4$–$CoMoO_4$,[14] $CoMoO_4$–MWCNTs,[9] and $CoMoO_4$–$NiMoO_4{\cdot}H_2O$.[15] Approximately 66% of the specific capacitance (1472 Fg^{-1}) at 5 mA cm^{-2} is retained even at the high current density of 20 mA cm^{-2}, suggesting high rate capability of the material. When increasing the current density, the capacitance value was decreased due to the decrease in charge diffusion to inner active sites.[11]

The EIS plots of $NiMoO_4$–$CoMoO_4{\cdot}xH_2O$ nanocomposites are displayed in Fig. 6. The curves show one semicircle in the high frequency region and a sloped line in the low frequency region. An internal resistance (R_b) value of all the composites is ~2.5 Ω. The charge transfer resistance (R_{ct}) is 1.9, 8.8 and 1.1 Ω for the samples with Ni–Co ratio 3 : 1, 1 : 1 and 1 : 3, respectively. The low resistance values indicate the high electronic conductivity of the synthesized samples. The lower

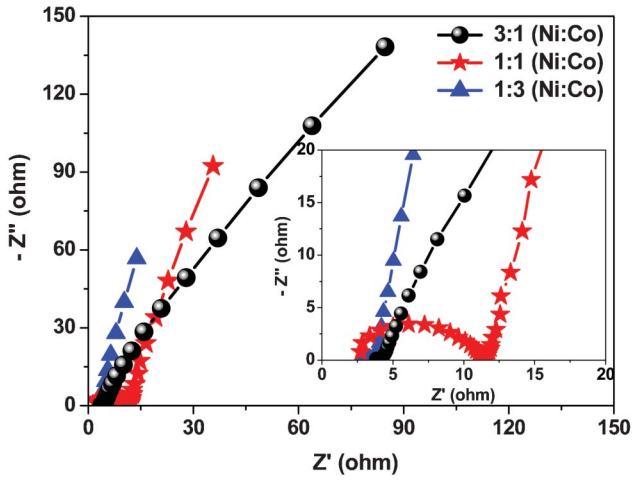

Fig. 6 Electrochemical impedance spectra (EIS) of combustion synthesized $NiMoO_4$–$CoMoO_4{\cdot}xH_2O$ nanocomposites.

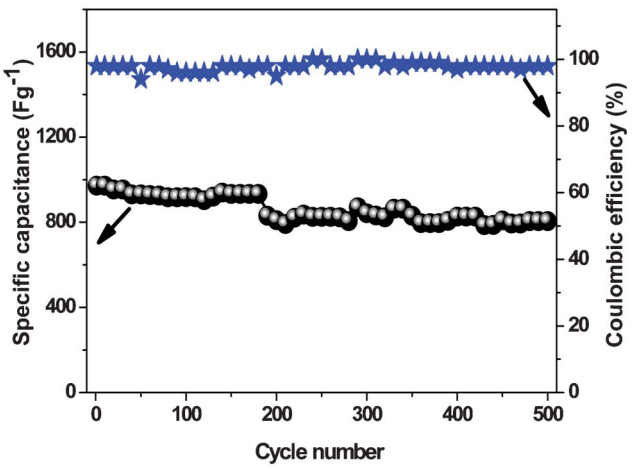

Fig. 7 Specific capacitance and coulombic efficiency *vs.* cycle number of the combustion synthesized $NiMoO_4$–$CoMoO_4{\cdot}xH_2O$ nanocomposite (3 : 1).

slope value for the sample with Ni–Co ratio 3 : 1 compared to other samples indicates a decrease in diffusion resistance.

The cycling stability of the 3 : 1 material was tested using the galvanostatic charge–discharge method at a current density of 20 mA cm^{-2} up to 500 cycles. The capacitance and coulombic efficiency calculated from the discharge curves is given in Fig. (7). Above 78% of the initial capacitance was retained even after 500 cycles, indicating good cycling stability compared to pure combustion synthesized $NiMoO_4$.[11] The enhancement in electrochemical performance of the composite (3 : 1) compared to combustion synthesized $NiMoO_4$, $CoMoO_4$[11] and other composites (1 : 1, 1 : 3) in this study is due to an increase in the surface area and active sites by the decrease in particle size and the synergistic effect of Ni and Co molybdates.[13–18] It is well documented that the electronic conductivity of nickel systems will be improved by the substitution of cobalt compounds.[29,30] Similarly the electrochemical performance of cobalt systems will be enhanced by the increase in active site density and roughness.[30,31] These synergistic effects of the composites is the reason for the enhancement in the electrochemical performance of the Ni–Co based composites.

Fig. 8(a) shows the cyclic voltammogram, recorded at various scan rates, of an asymmetric supercapacitor (AC||$NiMoO_4$–$CoMoO_4{\cdot}xH_2O$ (3 : 1)). The observed redox peaks confirmed the pseudo-capacitive charge storage in the cell. Electrolyte cation (Na^+) adsorption–desorption may be possible at the anode (AC), with the formation of an electrical double layer, facilitating the charge storage. The surface redox reactions due to the electrolyte anions (OH^-) are at the positive electrode; this produces the quasi-rectangular CV curves. The possible electrochemical reactions in the cell are, for the positive electrode, those shown in eqn (1) and for the negative electrode, as given below in eqn (2).[32]

Negative electrode

$$AC + xNa^+ + xe^- \leftrightarrow AC\,(xe^-) \,||\, xNa^+ \qquad (2)$$

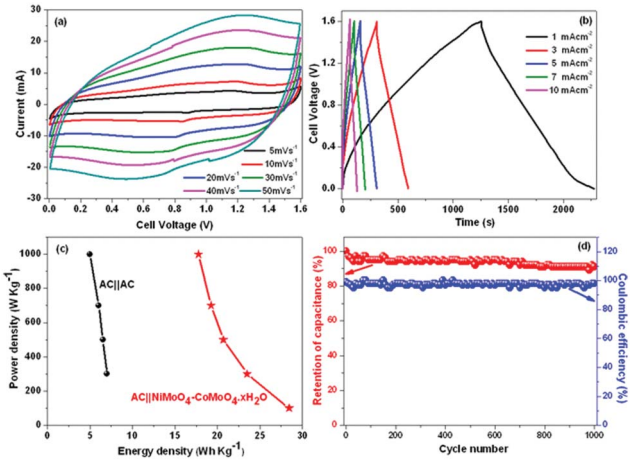

Fig. 8 CV curves of the full cell at various scan rates (a). Charge–discharge curves of the cell at various current densities (b). Ragone plots of the symmetric and asymmetric supercapacitor (c). Specific capacitance and coulombic efficiency *vs.* cycle number of the asymmetric full cell (d).

(here, || indicates double layer).

The galvanostatic charge–discharge cycles were performed at various current densities for the asymmetric cell, as given in Fig. 8(b). A quasi-symmetric profile, further supporting pseudo-capacitive behaviour, is evident. A small IR drop ($\sim$0.05 V at 1 mA cm^{-2}) was observed in the charge–discharge profile due to the equivalent series resistance (ESR) of the cell. The specific capacitance (C), energy density (E) and power density (P) of the full cell were calculated using the following formulas.

$$C = \frac{I}{m(\mathrm{d}v/\mathrm{d}t)} \quad (3)$$

$$E = i\int \frac{V\,\mathrm{d}t}{m} \quad (4)$$

$$P = \frac{E}{\Delta t} \quad (5)$$

where i is the current density, dv/dt is the average slope of the discharge curve, V the cell potential, Δt is the discharge time of the discharge curve and m is total mass of the positive and negative electrodes. The specific capacitance value obtained for the cell from Fig. 7(b) is 80, 66, 58, 54 and 50 Fg^{-1} at current densities 1, 3, 5, 7 and 10 mA cm^{-2}, respectively.

A Ragone plot for the symmetric and asymmetric cell is shown in Fig. 8(c). The asymmetric capacitor delivers an energy density of 28 Wh kg^{-1} at a power density of 100 W kg^{-1} and 18 Wh kg^{-1}, even at a high power density of 1000 W kg^{-1}. These cell capacitance and energy density values are significantly greater than the reported values for the AC||$CoMoO_4$–$NiMoO_4{\cdot}xH_2O$,[15] AC||Ni–Co oxide,[33] AC||Al–Co oxide,[34] AC||$(Ni_{1/3}Co_{1/3}Mn_{1/3})(OH)_2$,[32] AC||$Fe_3O_4$[35] and AC||$MnO_2$[36] asymmetric capacitors. The cycle life of the cell was investigated up to 1000 cycles. Fig. 8(d) shows that the capacitance retention (%) and coulombic efficiency of the cell obtained at 10 mA cm^{-1} tested for 1000 charge–discharge cycles.[2] Good coulombic efficiency (>95%) was observed for the asymmetric cell, capacitance is stable and above 92% of the capacitance was retained even up to 1000 cycles.

4. Conclusions

In summary, nano-sized β-$NiMoO_4$–$CoMoO_4{\cdot}xH_2O$ composites were successfully synthesized by a solution combustion synthesis (SCS) technique. The formation of β-$NiMoO_4$–$CoMoO_4{\cdot}xH_2O$ composites was identified by XRD. The EDS, elemental mapping and BET measurements showed stoichiometric elemental composition, uniform distribution of elements and pore size distributions of the composites, respectively. The $NiMoO_4$–$CoMoO_4{\cdot}xH_2O$ with the weight ratio of 3 : 1 (Ni : Co) delivered a maximum specific capacitance of 1472 F g^{-1} due to small particle size, uniform particle size distribution, high surface area, increase in electronic conductivity by the Co systems and high concentration of Ni. The synergistic effect of nickel and cobalt influence the overall electrochemical performance of the composites. The full cell (AC||$NiMoO_4$–$CoMoO_4{\cdot}xH_2O$) delivered a high specific capacitance (80 F g^{-1}) and energy density (28 Wh kg^{-1}), and good cycling stability up to 1000 cycles.

Acknowledgements

The Infrared analysis was undertaken in the FRIR beam line at the Australian Synchrotron, Victoria, Australia through grant no. AS123/HRIR/5428B.

Notes and references

1 R. Rangel, P. Bartolo-Perez, E. Martinez, X. A. Trejo-Cruz, G. Diaz and D. H. Galvan, *Catal. Sci. Technol.*, 2012, **2**, 847–852.
2 W-S. Wang, L. Zhen, C.-Y. Xu and W.-Z. Shao, *Cryst. Growth Des.*, 2009, **9**, 1558–1568.
3 Q. Dai, G. Zhang, P. Liu, J. Wang and J. Tang, *Inorg. Chem.*, 2012, **51**, 3232–3239.
4 D. M. Bubb, D. Cohen and S. B. Qadri, *Appl. Phys. Lett.*, 2005, **87**, 131909.
5 J. Haetge, I. Djerdj and T. Brezesinski, *Chem. Commun.*, 2012, **48**, 6726–6728.
6 Y. Dong, Y. Wan, Y.-L. Min, W. Zhang and S.-H. Yu, *Inorg. Chem.*, 2008, **47**, 7813–7823.
7 W. Xiao, J. S. Chen, C. M. Li, R. Xu and X. W. Lou, *Chem. Mater.*, 2010, **22**, 746–754.
8 K. K. Purushothaman, M. Cuba and G. Muralidharan, *Mater. Res. Bull.*, 2012, **47**, 3348–3351.
9 Z. Xu, Z. Li, X. Tan, C. M. B. Holt, L. Zhang, B. S. Amirkhiz and D. Mitlin, *RSC Adv.*, 2012, **2**, 2753–2755.
10 M.-C. Liu, L.-B. Kong, X.-J. Ma, C. Lu, X.-M. Li, Y.-C. LuO and L. Kang, *New. J. Chem.*, 2012, **36**, 1713–1716.

11 B. Senthilkumar, K. Vijaya Sankar, R. Kalai Selvan, M. Danielle and M. Manickam, *RSC Adv.*, 2013, **3**, 352–357.
12 Z.-Q. Liu, L.-Y. Tang, N. Li, K. Xiao, J. Wang, J.-H. Zhang, Y.-Z. Su and Y.-X. Tong, *J. Electrochem. Soc.*, 2012, **159**, D582–D586.
13 K.-S. Park, S.-D. Seo, H.-W. Shim and D.-W. Kim, *Nano Research Letters*, 2012, **7**, 35.
14 L.-Q. Mai, F. Yang, Y.-L. Zhao, X. Xu, L. Xu and Y.-Z. Luo, *Nat. Commun.*, 2011, **2**, 381.
15 M.-C. Liu, L.-B. Kong, C. Lu, X.-J. Ma, X.-M. Li, Y.-C. LuO and L. Kang, *J. Mater. Chem. A*, 2013, **1**, 1380–1387.
16 Y. Q. Wu, X. Y. Chen, P. T. Ji and Q. Q. Zhou, *Electrochim. Acta*, 2011, **56**, 7517–7522.
17 H. Jiang, T. Zhao, C. Yan, J. Ma and C. Li, *Nanoscale*, 2010, **2**, 2195–2198.
18 F.-L. Zheng, G.-R. Li, Y.-N. Ou, Z.-L. Wang, C.-Y. Su and Y.-X. Tong, *Chem. Commun.*, 2010, **46**, 5021–5023.
19 K. Rajeshwar and R. De Tacconi Norma, *Chem. Soc. Rev.*, 2009, **38**, 1984–1998.
20 C. Sekar, R. Kalai Selvan, S. T. Senthilkumar, B. Senthilkumar and C. Sanjeeviraja, *Powder Technol.*, 2012, **215–216**, 98–103.
21 P. S. Sathiskumar, C. R. Thomas and Giridhar Madras, *Ind. Eng. Chem. Res.*, 2012, **51**, 10108–10116.
22 W. Wen and J.-M. Wu, *Appl. Mater. Interfaces*, 2011, **3**, 4112–4119.
23 (*a*) B. Moreno, E. Chinarro, M. T. Colomer and J. R. Jurado, *J. Phys. Chem. C*, 2010, **114**, 4251–4257; (*b*) C. Mazzocchia, E. Tempesti and C. Aboumrad, *Fr. Patent* 89-00522, 1989.
24 J. A. Rodriguez, S. Chaturvedi, J. C. Hanson and J. L. Brito, *J. Phys. Chem. B*, 1999, **103**, 770–781.
25 V. Hangloo, S. Pandita, K. K. Bamzai, P. N. Kotru and N. Sahni, *Cryst. Growth Des.*, 2003, **3**, 753–759.
26 J.-W. Lang, L.-B. Kong, M. Liu, Y.-C. Luo and L. Kang, *J. Electrochem. Soc.*, 2010, **157**, A1341–A1346.
27 D. Klissurski, M. Mancheva, R. Iordanova, G. Tyuliev and B. Kunev, *J. Alloys compd.*, 2006, **422**, 53–57.
28 V. Srinivasan and J. W. Weidner, *J. Electrochem. Soc.*, 2000, **147**(3), 880–885.
29 (*a*) M. Oshitani, H. Yufu, K. Takashima, S. Tsuji and Y. Matsumaru, *J. Electrochem. Soc.*, 1989, **136**, 1590–1593; (*b*) J. Chen, D. H. Bradhurst, S. X. Dou and H. K. Liu, *J. Electrochem. Soc.*, 1999, **146**, 3606–3612.
30 J.-H. Zhong, A.-L. Wang, G.-R. Li, J.-W. Wang, Y.-N. Ou and Y.-X. Tong, *J. Mater. Chem.*, 2012, **22**, 5656–5665.
31 Y. Li, P. Hasin and Y. Wu, *Adv. Mater.*, 2010, **22**, 1926–1929.
32 Y. Zhao, Q. Y. Lai, Y. J. Hao and X. Y. Ji, *J. Alloys Compd*, 2009, **471**, 466–469.
33 C. Tang, Z. Tang and H. Gong, *J. Electrochem. Soc.*, 2012, **159**(5), A651–A656.
34 Y.-G. Wang, L. Cheng and Y.-Y. Xia, *J. Power Sources*, 2006, **153**, 191–196.
35 X. Du, C. Wang, M. Chen, Y. Jiao and J. Wang, *J. Phys. Chem. C*, 2009, **113**, 2643–2646.
36 A. Yuan and Q. Zhang, *Electrochem. Commun.*, 2006, **8**, 1173–1178.

